

Microwave Dielectric Properties of $\text{Ni}_{0.2}\text{Cu}_x\text{Zn}_{0.8-x}\text{Fe}_2\text{O}_4$ for Application in Antenna

Kumar Mohit^{1,*}, Vibha R. Gupta¹, and Sanjeeb K. Rout²

Abstract—Structural, vibrational and microwave dielectric properties of Nickel-Copper-Zinc ferrite ($\text{Ni}_{0.2}\text{Cu}_x\text{Zn}_{0.8-x}\text{Fe}_2\text{O}_4$) ceramics have been presented in this paper. Samples have been prepared using conventional auto-combustion method. The X-ray diffraction (XRD) results confirmed the ferrite samples to be of cubic spinel structure, which further was validated by Fourier transform infrared (FT-IR) and Raman spectroscopy. The relative permittivity (ϵ_r) increased from 7.474 to 8.132 with successive increase in Cu content. The observed and calculated permittivity using Clausius-Mossoitti relation have been in good agreement. The temperature coefficient of resonant frequency (τ_f) decreased from -75.85 ppm/ $^\circ\text{C}$ to -32.12 ppm/ $^\circ\text{C}$ with increase in successive Cu content. The relative permeability (μ_r) have been calculated by using the Nicholson-Ross-Weir conversion technique. Using $\text{Ni}_{0.2}\text{Cu}_{0.2}\text{Zn}_{0.6}\text{Fe}_2\text{O}_4$ sample the ferrite resonator antennas have been designed in three different shapes. The experimental and theoretical characteristics of the antennas have been compared and a good agreement has been achieved.

1. INTRODUCTION

In the last few decades ceramic based dielectric resonators (DRs) have been extensively utilized in different microwave communication systems [1–6]. A dielectric resonator antenna (DRA) is fabricated from low-loss microwave dielectric material, whose resonant frequency is predominantly a function of size, shape, and material permittivity. The DRA offers attractive features, such as low ohmic loss, low profile, small size, and wide impedance bandwidth when compared with the microstrip antenna [7]. However, as the permittivity increases, the frequency bandwidth of the antenna gets reduced [8, 9], leading to limitations in size reduction and trade off in performances. More recently it has been shown that the use of magneto-dielectric materials (i.e., material with both relative permittivity and relative permeability greater than unity) allows antenna miniaturization without reducing the frequency bandwidth [10, 11]. Magneto-dielectric material is one kind of dielectric material whose value of permeability can be varied in a large scale. It is different from conventional antenna designs until now are based on the dielectric which is just changed the permittivity. This makes antenna design simpler because only one parameter of dielectric coefficients affects to the antenna performance. But this limits the ease with which the performance of the antenna can be improved. Thus, magneto-dielectric material offers a larger number of parameters of dielectric to modify the performance of the antenna and some characteristics of antenna can be improved to satisfy the requirements of application [12].

Ferrites are technologically important materials as they are used in the fabrication of magnetic, electronic and microwave devices. Rapid growths in ferrite usage have been occasioned by a trend toward higher frequencies of operation in telecommunications and power electronic applications [7, 13]. Due to their excellent dielectric properties, ferrites possess the advantages of low loss and high power handling capability relative to semiconductors [14, 15].

Received 7 September 2013, Accepted 4 December 2013, Scheduled 6 December 2013

* Corresponding author: Kumar Mohit (kr.mohitverma@gmail.com).

¹ Department of Electronics and Communication Engineering, Birla Institute of Technology, Mesra, Ranchi 835215, Jharkhand.

² Department of Applied Physics, Birla Institute of Technology, Mesra, Ranchi 835215, Jharkhand.

Ferrites with low loss tangents (both dielectric and magnetic) are very useful in the design of miniaturized antenna and also to maintain the electrical dimensions (the electrical length is the product of the geometrical length of the medium and its refractive index) [16]. Also these are inexpensive, efficient, simple, and compact magnetic device structures, which require to be developed in order to be compatible with the semiconductor technology [17, 18].

For a better understanding of ferrite materials for microwave applications, a large number of studies have been carried out recently [19–21]. Many groups have attempted ferrite such as $\text{Ni}_{0.95-x}\text{Zn}_x\text{Co}_{0.05}\text{Fe}_{1.90}\text{Mn}_{0.02}\text{O}_4$ with $x = 0-0.25$ [22], Ni-Co ferrite [23], $\text{Y}_3\text{Fe}_5\text{O}_{12}$ and $\text{Gd}_3\text{Fe}_5\text{O}_{12}$ [7], $\text{Ni}_{0.2}\text{Co}_x\text{Zn}_{0.8-x}\text{Fe}_2\text{O}_4$ with $x = 0-0.8$ [24] etc. for antenna applications.

Again the performance of porous ferrite materials in their bulk form where the grain dimensions are in micrometer scales is limited to a few megahertz frequency. This is due to their higher electrical conductivity and domain wall resonance [25–28]. In the other hand, larger grain size leads to higher magnetic loss [29].

So, obtaining a microstructure with dense, uniform and small grain size is the key to obtain both low dielectric and magnetic losses enabling the material to work at higher frequencies [30]. One way to achieve this is by synthesizing the ferrite particles in nanometric scales before compacting them for sintering. When the size of the magnetic particle is smaller than the critical size for multi-domain formation, the particle is in a single domain state. Domain wall resonance is avoided, and the material can work at higher frequencies [29].

Several synthesize techniques have been reported to achieve ferrite nanoparticles [31–34]. Auto-combustion technique is one of the best techniques in terms of less energy consumption. Furthermore this technique has many other advantages like the resultant product show better chemical homogeneity, higher reactivity, limited agglomeration which reduce the losses in the ceramics [35–38]. Also it has been reported that the magnetic properties can be improved compared to conventional ceramic method [39] as the use of nanoparticles sized material significantly enhances the identification and microwave dielectric properties [40, 41].

Nickel-zinc ferrites are one of the most important soft ferrites whose high permeability and low power loss are the principal requirements for electronic devices [42]. They have great potential as microwave materials because of their high resistivity, ease of fabrication as well as low eddy current losses and high saturation magnetization as compared with other ferrites [43–48]. Variations in the zinc concentration in these ferrites allow the tailoring of the magnetic properties to suit the requirement of a particular application [49]. Substitution of Copper in these ferrites has been known to improve the sintering properties drastically [50, 51].

Furthermore, the microwave dielectric and magnetic properties of the Cu substituted Ni-Zn-Ferrites are rare. Few reports are available on the applicability of these materials as microwave absorber [52]. Here, this paper presents the structural as well as microwave dielectric and magnetic properties of $\text{Ni}_{0.2}\text{Cu}_x\text{Zn}_{0.8-x}\text{Fe}_2\text{O}_4$ ($x = 0, 0.2, 0.4, 0.6$ and 0.8) nanoparticles synthesized by auto-combustion synthesis. Resonator antenna behavior of $\text{Ni}_{0.2}\text{Cu}_{0.2}\text{Zn}_{0.6}\text{Fe}_2\text{O}_4$ ceramic has been accounted for base station applications in cylindrical, cuboid, and triangular geometry.

2. EXPERIMENTAL PROCEDURE AND CORE MATHEMATICS

2.1. Synthesis of Ni-Zn-Cu Ferrite Nanoparticles by Auto-combustion Reaction

High pure (99.99%, Merck India Chemicals) analytical grade reagents, Nickel nitrate, Zinc nitrate, Copper nitrate, Ferric nitrate and Citric acid were used in the synthesis of $\text{Ni}_{0.2}\text{Cu}_x\text{Zn}_{0.8-x}\text{Fe}_2\text{O}_4$ (NCZFO) nanoparticles. Stoichiometric proportions of the nitrate salts were taken for the preparation of NCZFO nanoparticles. Aqueous solution of nitrate salts and citric acid were prepared in distilled water with continuous stirring using a magnetic stirrer at room temperature. The prepared aqueous solution of nitrate salts were mixed together with continuous stirring. The mixed nitrate solution was added to citric acid solution under constant stirring for 2 h at room temperature in ambient atmosphere, resulting in precursor solution. The molar ratio of nitrates to citric acid was maintained at 1 : 1. Small amount of ammonia hexahydrate solution was added into the precursor solution to bring the pH ~ 7 . The precursor of complex metal ions was heated at 70°C for 20 h to obtain gel. Further, heating of

the gel ($\sim 100^\circ\text{C}$) lead to auto-combustion, producing loose powder of the NCZFO [53]. The NCZFO powders were calcined at 500°C for 4 h and used for characterization.

2.2. Structural and Micro Structural Characterizations

The ferrite powders were characterized for phase identification, crystallite size and lattice parameter determination using X-ray diffraction (Bruker D8-advance X-Ray Diffractometer) with Cu K_α radiation. The crystallite size was calculated from peak broadening using Scherrer formula

$$D_{hkl} = \frac{0.9\lambda}{\beta \cos \theta} \quad (1)$$

where $D_{h,k,l}$ is the crystallite size perpendicular to $(h k l)$ plane, λ the wavelength of X-ray used, β (rad.) the FWHM of the diffraction peak, and θ the peak position. The X-ray density (ρ_x) of the samples was calculated using the relation given by Smit and Wijn [54, 55]:

$$\rho_x = nM/N_A a^3 \quad (2)$$

where M is the molecular weight of the samples, N_A the Avogadro's number, n the number of formula unit present in a unit cell (in the present case, $n = 8$), and a the lattice parameter. X ray density (ρ_x) was calculated using Eq. (2) and found to be in the range of 5.948 to 6.012 g/cm³. Fourier transform infrared spectroscopy (FTIR) (IR-Prestige-21) was used to study chemical structure changes. Raman studies were performed using a spectrometer (Jobin-Yvon T64000 Spectrometer) with an excitation wavelength of 514.5 nm, from an Ar laser. The monophasic powder samples were granulated with PVA as binder and were uniaxially pressed using steel die of different geometry. The sample $\text{Ni}_{0.2}\text{Zn}_{0.8}\text{Fe}_2\text{O}_4$ was sintered at 1200°C , while sintering of substituted ferrites was performed at various temperatures in the range 950°C to 1000°C in air environment to obtain the bulk density to about 95% of their respective x-ray density. The bulk density of the sintered samples was calculated using Archimede's principle. The grain size and grain morphology of the sintered NCZFO were studied using scanning electron microscopy (SEM) on a Zeiss DSM 982 Gemini instrument with a Schottky emitter at an accelerating voltage of 2 kV and a beam current of 1 μA .

2.3. Microwave Dielectric Constant Measurements

Microwave dielectric measurements were performed using a Vector Network Analyzer (N5230A Agilent Technologies, USA) in a $\text{TE}_{01\delta}$ mode of cylindrical shaped NCZFO. $\text{TE}_{01\delta}$ resonance mode using Hakki-Coleman [56] dielectric resonator method as modified and improved by Courtney [57]. This is a mode at which we have measured the dielectric properties of samples. Other modes can also be used but this is more appropriate mode as proposed by Sebastian et al. [58] and Krupka et al. [59, 60]. The quality factor (Q), permittivity (ϵ) and temperature coefficient (τ_f) of the DRs can be measured using a transmission mode cavity proposed by Krupka et al. [59, 60]. The dielectric resonator is placed inside a cylindrical metallic cavity usually made of copper and the inner surfaces are finely polished and usually gold or silver coated. The cavity is closed with a lid after loading the dielectric resonator sample. Microwave is fed using loop coupling. The electric field is symmetric with the geometry of the sample and the cavity, which helps to reduce the sources of loss due to cavity. A schematic diagram of the experimental setup is shown in Fig. 1. In the $\text{TE}_{01\delta}$ mode, the field confinement is not complete in the z -direction and hence TE_{011} mode is designated as $\text{TE}_{01\delta}$. This mode is widely used in materials property characterization because in this mode there is no current crossing the dielectric and the conducting plates. So possible air gaps between the dielectric and the conducting plates have no effects on resonance properties of this mode [61]. The theoretical model is properly described for the configuration mentioned by Courtney and as modified from Kobayashi and Tanaka [62]. The $\text{TE}_{01\delta}$ resonance mode has been found most suitable for the real part of the relative dielectric constant (ϵ_r). A gain/loss factor ($\tan \delta$) of the specimen could be obtained from the measured resonance frequency (f_r) and unloaded quality factor (Q_0) for the $\text{TE}_{01\delta}$ resonance mode [9, 63].

The relative dielectric constant and loss factors were calculated using the following formula [56]:

$$r = 1 + \left(\frac{c}{\pi D f_r} \right) (\alpha^2 + \beta^2) \quad (3)$$

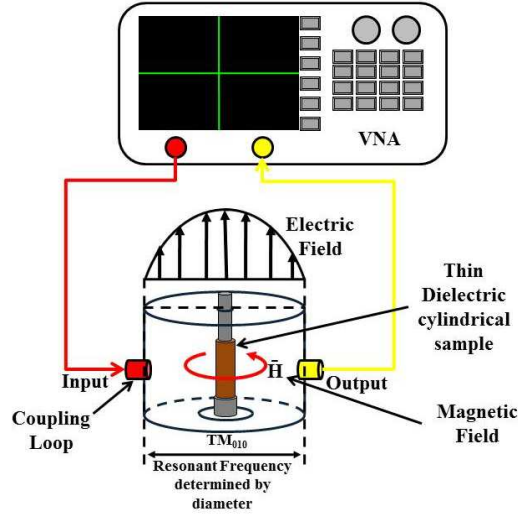


Figure 1. Schematic diagram of measurement setup for resonant frequency and S -parameter using cavity resonator.

where, c is the velocity of light, α is given by the mode chart [64] and β is obtained from the resonance frequency (f_r) and the sample dimension. The $\tan \delta$ is given by Hakki-Coleman [56] as described in Eq. (4):

$$\tan \delta = \frac{A}{Q_u} - BR_s \quad (4)$$

Here,

$$A = 1 + \frac{W}{\epsilon_r} \quad (5)$$

$$B = \left(\frac{l\lambda}{2L} \right)^3 \frac{1+W}{30\pi^2\epsilon_r l} \quad (6)$$

$$W = \frac{J_1^2(\alpha_1)}{K_1^2(\beta_1)} \cdot \frac{K_0(\beta_1)K_2(\beta_1) - K_1^2(\beta_1)}{J_1^2(\alpha_1) - J_0(\alpha_1)J_2(\alpha_1)} \quad (7)$$

$$R_s = \sqrt{\frac{\pi f_r \mu}{\sigma}} \quad (8)$$

The function W is the ratio of electric field energy stored on the outside of the rod to the energy inside the rod. The λ is the free-space wavelength, L the length of the dielectric specimen, and $l =$ an integer (1, 2, 3, 4, ...). The σ is the conductivity of the shorting plate, and Q_0 is the unloaded quality factor of the dielectric resonator. If the dielectric material is isotropic then the characteristic equation for such a resonance structure for the TE_{011} mode is given by Eq. (9):

$$\alpha \frac{J_0(\alpha)}{J_1(\alpha)} = -\beta \frac{K_0(\beta)}{K_1(\beta)} \quad (9)$$

where, $J_0(\alpha)$ and $J_1(\alpha)$ are the Bessel functions of the first kind of order zero and one, respectively. $K_0(\beta)$ and $K_1(\beta)$ are the modified Bessel functions of the second kind of orders zero and one, respectively.

Kobayashi and Katoh [65] described a method for the experimental determination of R_s which employs two rod samples cut from the same dielectric rod with equal diameters but different lengths. The rod for a TE_{01l} resonator is “ l ” times as long as the other rod for a TE_{011} resonator, where $l \geq 2$. Here subscripts l and 1 are denoted as quantities for both resonators, respectively. Because of the different conduction loss contributions in the two cases, the modes have almost the same resonance

frequency but differ in unloaded Q ; i.e if $f_{0l} = f_{01}$, then $Q_{0l} > Q_{01}$. Because both rods have the same ($\tan \delta$), the expression for (R_s) is given by Eq. (10) [62]:

$$R_s = 30\pi^2 \left(\frac{2L}{l\lambda}\right)^3 \cdot \frac{\varepsilon_r + W}{1 + W} \cdot \frac{l}{l-1} \cdot \left(\frac{1}{Q_{01}} - \frac{1}{Q_{0l}}\right) \quad (10)$$

Then substitution of Eq. (10) into Eq. (4) yields:

$$\tan \delta = \frac{A}{l-1} \left(\frac{1}{Q_{0l}} - \frac{1}{Q_{01}}\right) \quad (11)$$

This calculation facilitates the precise measurement of ($\tan \delta$). The quality factor ($Q \times f$) was measured using a reflection mode gold-coated copper cavity [9].

The τ_f value of samples was measured by introducing the cavity in temperature controlled chamber using the following equation:

$$\tau_f = \left(\frac{1}{f}\right) \left(\frac{\Delta f}{\Delta T}\right) \quad (12)$$

2.4. Calculation of Microwave Magnetic Constant

Microwave permeability was calculated by the Nicholson-Ross-Weir conversion technique using S -parameters that was recorded by Vector Network Analyzer in a TM_{010} resonance mode. This method provides a direct calculation of both the permittivity and permeability from S -parameters [66].

This is the most commonly used method for performing such conversion. Measurement of reflection coefficient and transmission coefficient requires all four (S_{11} , S_{21} , S_{12} , S_{22}) or a pair (S_{11} , S_{21}) of S -parameter of the material to be measured. The present calculation for permeability includes only S_{11} and S_{21} parameter which is shown below.

The transmission and reflection co-efficient are related to S -parameter as per following formula [66, 67]:

$$T = \frac{S_{11} + S_{21} - \Gamma}{1 - (S_{11} + S_{21})\Gamma} \quad (13)$$

$$\Gamma = X \pm \sqrt{X^2 - 1} \quad (14)$$

where,

$$X = \frac{S_{11}^2 - S_{21}^2 + 1}{2S_{11}} \quad (15)$$

Here, Γ is reflection co-efficient; T is transmission co-efficient, and S_{11} and S_{21} are reflection loss and insertion loss, respectively.

The free space wavelength (λ_0), cut-off wave length (λ_c) are related to transmission coefficient and diameter of cylindrical shaped sample as (16):

$$\frac{1}{\Lambda^2} = \left(\frac{s_r \mu_r}{\lambda_0^2} - \frac{1}{\lambda_c^2}\right) = -\left(\frac{1}{2\pi L} \ln\left(\frac{1}{T}\right)\right)^2 \quad (16)$$

The permeability can be calculated by using the formula:

$$\mu_r = \frac{1 + \Gamma}{\Lambda(1 - \Gamma)\sqrt{\frac{1}{\lambda_0^2} - \frac{2}{\lambda_c^2}}} \quad (17)$$

By substituting Eq. (16) in Eq. (17), we obtain a quadratic Equation in terms of permeability (μ_r),

$$(1 + \Gamma^2 - 2\Gamma) \left(\frac{1}{\lambda_0^2} - \frac{1}{\lambda_c^2}\right) \mu_r^2 \left((1 + \Gamma^2 + 2\Gamma) \frac{s_r}{\lambda_0^2}\right) \mu_r + (1 + \Gamma^2 + 2\Gamma) \frac{1}{\lambda_c^2} = 0 \quad (18)$$

The permeability of the NCZFO samples was calculated by solving the above equation.

2.5. Ferrite Resonator Antenna (FRA) Measurements

The sintered cylindrical, cuboid and triangular shaped $\text{Ni}_{0.2}\text{Cu}_{0.2}\text{Zn}_{0.2}\text{Fe}_2\text{O}_4$ ceramic were used for the resonator antenna study. The schematic diagram of the FRA is given in the Fig. 2.

The ferrite resonators are excited by coaxial cable. The FRA is placed above a conducting ground plane made of FR4 sheet with copper coating on both side. The outer conductor of a subminiature version A (SMA) connector is connected to the ground plane and the inner conductor (probe) is connected to the Ferrite resonator (FR). The probe is located at $x = 6.35 \text{ mm}$ and $\varphi = 0^\circ$ as shown in Fig. 2. A fixed dimension of ground plane ($L \times W \times T = 100 \text{ mm} \times 100 \text{ mm} \times 1.6 \text{ mm}$) and coaxial probe of different length are used for all shaped FRA. The probe length is optimized to obtain with respect to the $\text{Ni}_{0.2}\text{Cu}_{0.2}\text{Zn}_{0.6}\text{Fe}_2\text{O}_4$ composition for each geometry of FRA for impedance matching. However this impedance match can also be adjusted by changing the probe length with respect to the other compositions. The composition $\text{Ni}_{0.2}\text{Cu}_{0.2}\text{Zn}_{0.6}\text{Fe}_2\text{O}_4$ is chosen as a representative (for briefness only) one due to its highest quality factor (lowest dielectric loss) and lowest magnetic loss among all the Cu containing compositions.

In the case of cylindrical FRA, the probe adjacent to the FRA can excite the basic mode, $\text{HE}_{11\delta}$ mode [9], whose resonant frequency f_r can be approximated by [6, 68]

$$f_r = \frac{2.997 \times 10^8}{2\pi\sqrt{\epsilon_r\mu_r}} \sqrt{\left(\frac{1.841}{r}\right)^2 + \left(\frac{\pi}{2h}\right)^2} \quad (19)$$

where μ_r is the real part of permeability and ϵ_r the real part of permittivity. The cylindrical FRA under consideration has height, $h = 6.48 \text{ mm}$, and radius, $r = 6.35 \text{ mm}$. The Eq. (19) is obtained with the hypothesis that the lateral and upper surface of the ferrite resonator is perfectly magnetic conductor (PMC). Since this assumption is verified only for infinite permittivity, it is only an approximation that leads to some 10% error [7].

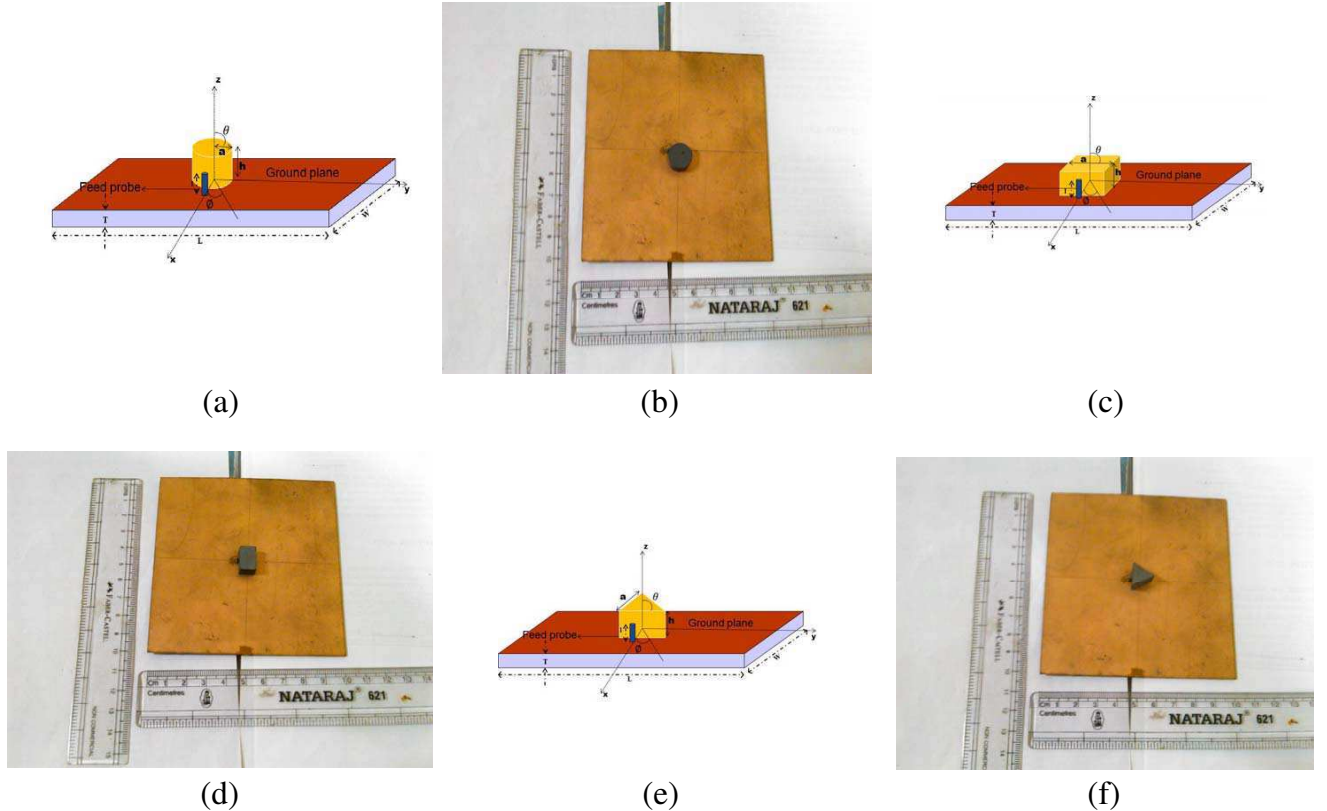


Figure 2. The schematic representation and photograph of, (a), (b) cylindrical, (c), (d) cuboid and (e), (f) triangular shaped FRA.

A comparison of the values from above equation to the following closed form of expression for the $HE_{11\delta}$ resonance frequency has been already published [69]:

$$f_r = \frac{6.324c}{2\pi r\sqrt{2 + \varepsilon_r\mu_r}} \left(0.27 + 0.36\frac{r}{2h} + 0.02\left(\frac{r}{2h}\right)^2 \right) \quad (20)$$

where the f_r is given in GHz, and c is the velocity of light. It has been observed that there is variation in simulation and measured results depends on the probe. This problem finds its origin in the air gap between the DR and metallic conductor which has been thoroughly studied by Junker et al. [70, 71].

In the case of a cuboid shape the probe adjacent to FRA excite the basic mode, TE_{111}^Y mode, whose resonant frequency f_r can be approximated by [72, 73]:

$$f_r = \frac{k_0c}{2\pi} \quad (21)$$

where, $k_x^2 + k_y^2 + k_z^2 = k_0^2\varepsilon_r\mu_r$, and k_x, k_y, k_z are given by

$$k_x = \frac{\pi}{a}, \quad k_z = \frac{\pi}{2h} \quad (22)$$

and

$$k_y \tan\left(\frac{k_y b}{2}\right) = \sqrt{(k_x^2 + k_z^2 - k_0^2)} \quad (23)$$

where, k_x, k_y and k_z represent the mode wave numbers inside the dielectric resonator, and k_0 is the free-space wave number. Cuboid shaped FRA under consideration has the length, $a = 9.7$ mm, width, $b = 14.5$ and height, $h = 6.52$ mm.

In the case of an equilateral-triangular FRA, resonance frequency of the excited mode TM_{mnl} is approximately given by [74, 75]

$$f_r = \frac{c}{\sqrt{\varepsilon_r\mu_r}} \left[\left(\frac{4}{3a}\right)^2 (m^2 + n^2 + mn) + \left(\frac{1}{2h}\right)^2 \right] \quad (24)$$

where, a is the length of each side of the triangle and h is the height of the resonator. The indices m, n and l should satisfy the condition $l + m + n = 0$ but they all cannot be zero simultaneously. For low profile resonators where $a \gg h$, this expression can be further simplified as

$$f_r = \frac{c}{4h\sqrt{\varepsilon_r\mu_r}} \quad (25)$$

The designed triangular FRA has the height, $h = 6.37$ mm and side, $a = 9.9$ mm.

The impedance bandwidth (return loss < -10 dB) were measured for all FRA using the following relation [76].

$$BW(\%) = \left(\frac{OR}{CF}\right) \times 100 \quad (26)$$

where, BW is the bandwidth, OR the operating range, and CF the center frequency.

3. RESULTS AND DISCUSSION

3.1. X-ray Diffraction Study

The room temperature X-ray diffraction patterns of NCZFO samples are shown in Fig. 3. The patterns indicate a single phase cubic spinal crystal structure with space group of $Fd\bar{3}m$. The sharp and intense peaks show the crystalline nature of the samples.

The lattice parameter of NCZFO ferrites is determined by using the formula [77];

$$a = \frac{\lambda}{2} \left(\frac{h^2 + k^2 + l^2}{\sin\theta} \right), \quad (27)$$

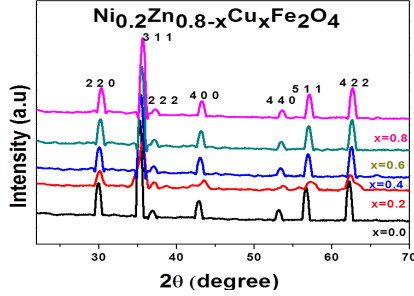


Figure 3. Room temperature XRD patterns of NCZFO samples.

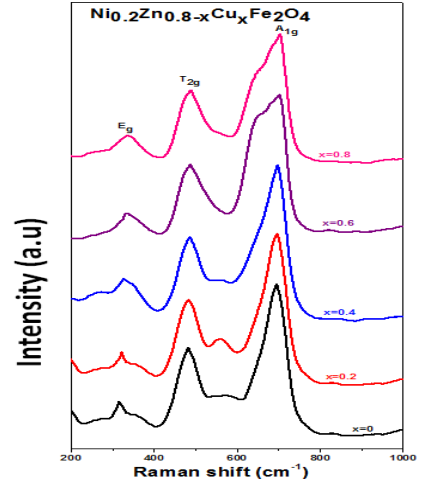


Figure 4. Room temperature Raman spectrum of NCZFO samples.

where $(h k l)$ are the Miller indices, and θ is the diffraction angle corresponding to the $(h k l)$ plane. From Fig. 3, it is observed that the diffraction peaks shift towards higher angles, which confirm that unit cell volume decreases with successive Cu substitution. The lattice parameter of the ferrites decreases from 0.812 nm to 0.8074 nm with increase in successive Cu^{2+} ion content. This result suggests a formation of a solid solution. This decrease in lattice parameter can be attributed to the substitution of the smaller radii Cu^{2+} (0.072 nm) ions at the larger Zn^{2+} (0.074 nm) ionic site [78, 79]. The little-bit random disorder may be due to formation of Fe^{2+} ions instead of Fe^{3+} ions on octahedral site [53, 80]. Scherrer's equation (Eq. (1)) is used for calculating the crystallite size from the X-ray diffraction data [54, 81] and is found to be in the range of 12–9 nm.

3.2. Raman Study

Raman spectroscopy is a non-destructive material characterization technique and is very sensitive to structural disorder. It provides an important tool to probe the surface and structural properties of materials. The Raman spectra of all samples in the frequency range $200 \sim 1000 \text{ cm}^{-1}$ at room temperature are shown in Fig. 4. There are three first-order Raman active modes ($A_{1g} + E_g + T_{2g}$), and all these modes are observed at ambient conditions. All the vibration frequencies for different compositions are presented in Table 1. The A_{1g} mode is due to symmetric stretching of oxygen atoms along Fe-O bonds, E_g mode are due to symmetric bending of oxygen with respect to Fe and T_{2g} mode is due to asymmetric stretching of Fe [82]. Here, the notation A is for one dimensional representation, E for two and T for three dimensional representations, g denotes the symmetry with respect to the center of inversion [83]. In cubic spinels including ferrites, modes at above 600 cm^{-1} generally correspond to the motion of oxygen in tetrahedral group (A-site) [84], and the other low frequency modes represent the characteristics of the octahedral group (B-site) of ferrites [53].

3.3. Fourier Transformed Infrared Analysis

The FTIR spectra shown in Fig. 5, confirms the formation of the spinel structure. In ferrites metal ions are situated at two different sub-lattices designated as tetrahedral (A-site) and octahedral (B-site) according to the geometrical configuration of the oxygen nearest neighbors. The high frequency band ν_1 is observed in the range from 576.5 to 584.3 cm^{-1} , associated with the A-site, while the low frequency band ν_2 is observed in the range 420.4 to 414.6 cm^{-1} associated with the octahedral B-site (Table 1). Waldron [85] and Hafner [86], attributed the ν_1 band to the intrinsic vibrations of the tetrahedral groups, the ν_2 band to the octahedral groups. Similar vibrations have also been observed by Zahi [42] at $\sim 570 \text{ cm}^{-1}$, assigned to tetrahedral bond stretching and the band at $\sim 418 \text{ cm}^{-1}$, assigned to the vibration in the octahedral site of the composition $\text{Ni}_{0.5}\text{Zn}_{0.5}\text{Fe}_2\text{O}_4$.

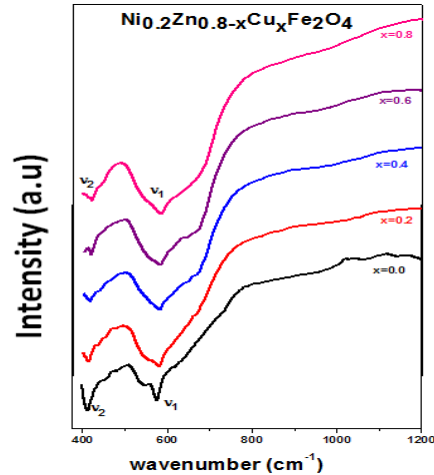


Figure 5. Room temperature FTIR spectra of NZFO samples.

Table 1. Selected peak positions of NCZFO obtained from Raman spectra and FTIR spectra.

Compositions	Raman Spectra			FTIR Spectra	
	Tetrahedral sites modes (cm ⁻¹)	Octahedral sites modes (cm ⁻¹)		Tetrahedral Peak Position (cm ⁻¹)	Octahedral Peak Position (cm ⁻¹)
	A _{1g}	T _{2g}	E _g		
Ni _{0.2} Zn _{0.8} Fe ₂ O ₄	696.3	483.5	315.8	576.5	414.6
Ni _{0.2} Cu _{0.2} Zn _{0.6} Fe ₂ O ₄	697.9	484.3	323.4	577.3	415.9
Ni _{0.2} Cu _{0.4} Zn _{0.4} Fe ₂ O ₄	700.1	487.8	328.6	579.7	417.5
Ni _{0.2} Cu _{0.6} Zn _{0.2} Fe ₂ O ₄	702.6	489.5	333.7	582	418.3
Ni _{0.2} Cu _{0.8} Fe ₂ O ₄	703.8	491.1	337.2	584.3	420.4

From Fig. 5, it is also observed that the absorption bands shift toward higher wave numbers with increase in Cu-content (Table 1). This shifting of peaks toward higher or lower wave number can be correlated with the formation of shorter and stronger M-O bonds in the ceramics [9,87]. Shifting of absorption peaks toward higher wave number with successive Cu substitution can be attributed to a change in lattice parameter, as the radius of Cu²⁺ is smaller than that of Zn²⁺ ion. Since the distance between Cu²⁺ ion and O₂²⁻ ion is smaller than the distance between Zn²⁺ ion and O₂²⁻ ion so the interaction between Cu-O becomes stronger than that of Zn-O. Therefore the bond strength of Zn-O is less than that of Cu-O. Likewise successive increase in Cu content, which does not induces much O-vacancies, promotes shifting of peaks toward higher wave number gradually.

3.4. Scanning Electron Microscope Study

Figure 6 shows the SEM images of NCZFO ceramics sintered at 1000°C. From figures, it is observed that the various size and shape of grains distributed homogeneously. The grain size was estimated by drawing random lines of known length and counting the number of grains along each line. The average grain size of the sintered samples is found to be in the range of 8–20 μm.

3.5. Microwave Dielectric and Magnetic Studies

The storage capacity for electric and magnetic energy is due to polarization of electrical and magnetic dipoles. Storage capacity of ferrites increases with increase in the value of the real part of dielectric

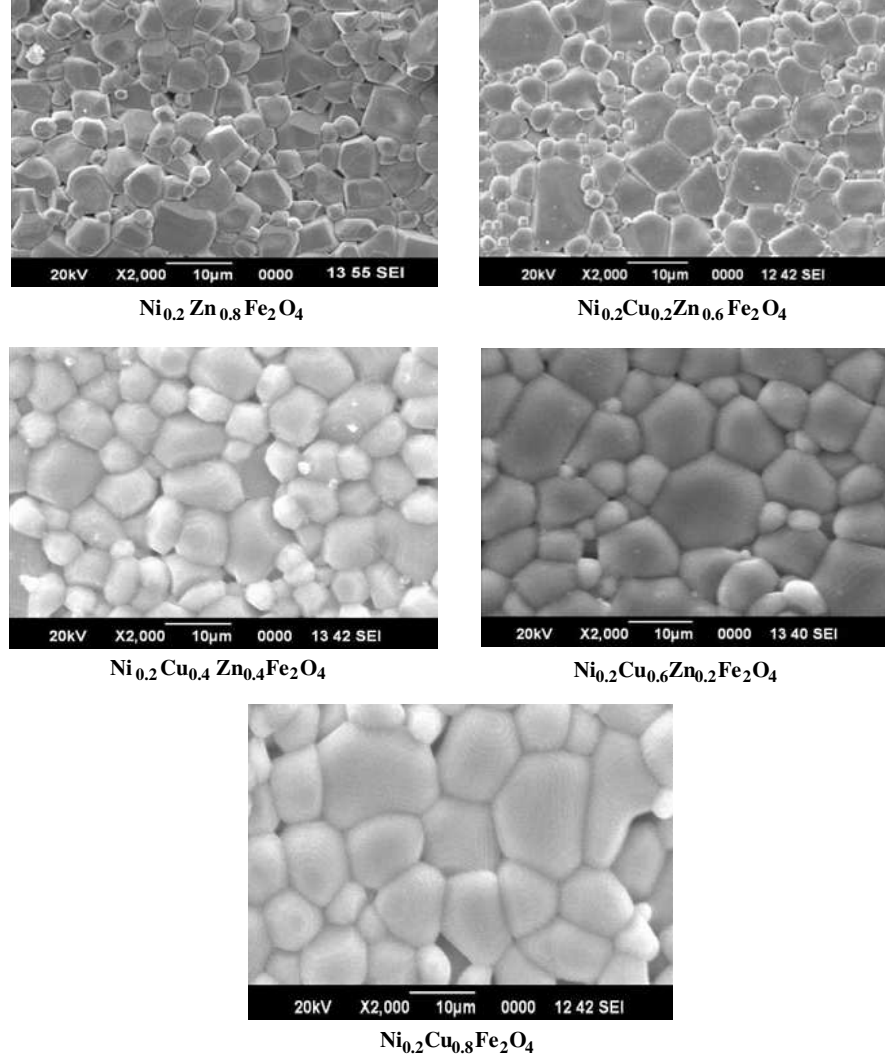


Figure 6. Scanning electron micrographs of NCZFO ceramics.

and magnetic constant. The real part of permittivity (ϵ'), i.e., dielectric constant, is directly dependent on electric polarizations [9, 88]. A low dielectric constant is mainly due to low ionic polarizability [89]. Shannon [90], suggested that molecular polarizabilities of complex substances could be broken up into the polarizabilities of constituent ions. In the case of spinel ferrite (AFe_2O_4), molecular polarizability can be estimated from following equation.

$$\alpha(\text{AB}_2\text{O}_4) = \alpha(\text{A}^{2+}) + 2\alpha(\text{Fe}^{3+}) + 4\alpha(\text{O}^{2-}) \quad (28)$$

where α is the polarizability. The dielectric constants of AFe_2O_4 compounds can be calculated from Clausius-Mosotti relation [90].

$$\epsilon_r^{Th} = \frac{3V_m + 8\pi\alpha}{3V_m - 4\pi\alpha} \quad (29)$$

where V_m is molar volume. Molar volume of AFe_2O_4 was calculated with the unit cell parameters determined from the diffraction pattern. The value of the dielectric constants (ϵ_r^{Th}) for NCZFO was calculated as per Shannon's suggestion. The value of polarizability of Ni^{2+} , Zn^{2+} , Cu^{2+} , Fe^{3+} and O^{2-} were taken to be 1.23, 2.04, 2.11, 2.29 and 1.21, respectively [58, 91]. The calculated permittivity (ϵ_r^{Th}) of NCZFO compounds along with the observed permittivity, corrected permittivity (ϵ_r^{corr}) after porosity correction and the value of porosity are shown in Table 2. The porosity correction was applied

for observed permittivity as per the relation, $\varepsilon_r^{corr.} = \varepsilon_r(1 + 1.5P)$, where P is apparent porosity [92]. The calculated and observed permittivity after porosity correction show good agreement. Microwave dielectric loss is mainly characterized by lattice-vibrational modes, number of pores, second any phases, impurities, lattice defects and also by density. The values of permeability (μ_r) of NCZFO were calculated by the Nicholson-Ross-Weir conversion process. The loss parameters could be related to the grain morphology. In the present case the low losses may be due to high density of the sintered ceramics that was resulted from the defect free materials produced in this auto combustion route. It is also observed that the sintering temperature of ceramics reduced from 1200°C to 1000°C with agreeable values of densities (see Table 2) on substitution of Cu in $\text{Ni}_{0.2}\text{Zn}_{0.8}\text{Fe}_2\text{O}_4$.

Table 2. The bulk density, apparent porosity and microwave dielectric properties of sintered NCZFO disks.

	$\text{Ni}_{0.2}\text{Zn}_{0.8}\text{Fe}_2\text{O}_4$	$\text{Ni}_{0.2}\text{Cu}_{0.2}\text{Zn}_{0.6}\text{Fe}_2\text{O}_4$	$\text{Ni}_{0.2}\text{Cu}_{0.4}\text{Zn}_{0.4}\text{Fe}_2\text{O}_4$	$\text{Ni}_{0.2}\text{Cu}_{0.6}\text{Zn}_{0.2}\text{Fe}_2\text{O}_4$	$\text{Ni}_{0.2}\text{Cu}_{0.8}\text{Fe}_2\text{O}_4$
Density (gm/cm ³)	5.724	5.751	5.679	5.607	5.545
App. Porosity (P)	0.063	0.061	0.065	0.058	0.057
ε_r^{Th}	8.244	8.407	8.591	8.713	8.825
ε_r	7.474	7.651	7.811	7.975	8.132
$\varepsilon_r^{corr.}$	8.18	8.351	8.573	8.669	8.778
$\tan \delta$	0.00193	0.00345	0.00359	0.00372	0.00379
μ_r	2.1085	2.3737	2.4962	2.6017	2.7138
$\tan \delta_m$	0.1029	0.1047	0.1076	0.1114	0.1146
$Q \times f_r$ (GHz)	2179.372	2241.822	2127.246	2082.573	2021.469
Γ_f (ppm/°C)	-75.85	-64.51	-52.53	-45.05	-32.12

It is observed that permeability (μ_r) increases with increase in successive Cu-content in NCZFO. This increase might be due to greater value of susceptibility of Copper than Zinc [93]. The degradation of $Q \times f_r$ value can be attributed to the decrease in density due to the inhomogeneous grain growth as well as evaporation of Zn [94].

Temperature co-efficient of resonant frequency, (τ_f) is expressed by thermal expansion coefficient, α_1 and temperature co-efficient of permittivity, (τ_ε) as follows:

$$\tau_f = -\alpha_1 - \tau_\varepsilon \quad (30)$$

The thermal expansion co-efficient of a ceramic is generally in the range of 10 ppm/°C, therefore the sign and the magnitude of (τ_f) depends on (τ_ε). Since the unit cell volume has a strong correlation with lattice energy, (τ_ε) is proportional to the relative magnitude of unit cell volume. So, the magnitude of (τ_ε) increases as the unit cell volume increase provided the structure remains same [92]. This is in consistent with our XRD data.

3.6. Ferrite Resonator Antenna Study

In this section, the proposed FRA, designed using cylindrical, cuboid and triangular shaped samples of $\text{Ni}_{0.2}\text{Cu}_{0.2}\text{Zn}_{0.6}\text{Fe}_2\text{O}_4$ is reported. For an antenna to work efficiently there should be proper impedance matching between an antenna and its feed. The impedance matching in an antenna is measured in terms of return loss or the scattering parameter S_{11} which represents the power reflected back into the feed (in transmitting mode). In the case of probe fed FRA, S_{11} as a function of frequency is analyzed for different lengths of coaxial probe. It is observed that the coupling between the probe and FRA can be controlled by varying the probe length (l). The optimized impedance matching is obtained for $l = 6.35$ mm, 6.15 mm and 6.25 mm for the cylindrical, cuboid and triangular FRA respectively. The reflection loss characteristics for the FRA under consideration are shown in Fig. 7. The parametric study of the return loss with respect to probe length l is also shown in the same figure.

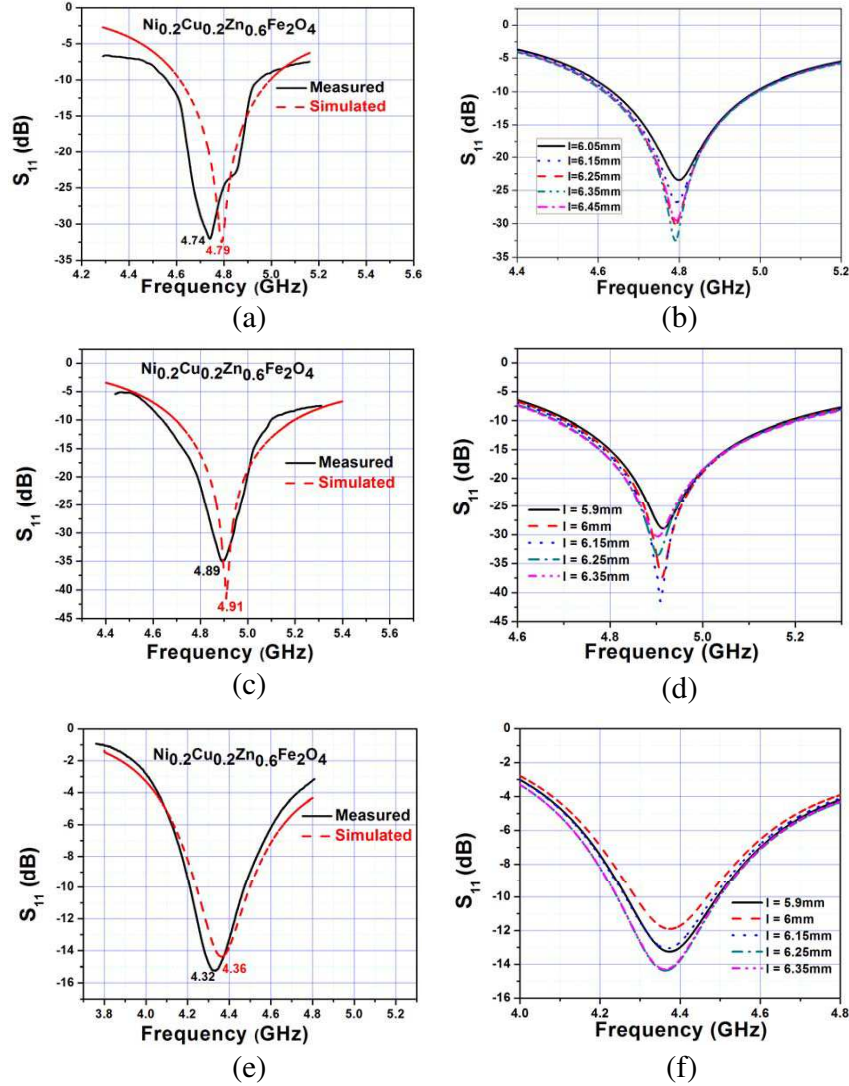


Figure 7. Simulated and measured return loss (S_{11}) with optimum probe length and variation of simulated S_{11} for different probe lengths for: (a), (b) cylindrical FRA, (c), (d) cuboid FRA and (e), (f) triangular FRA.

The radiation pattern is the graphical representation of radiation properties, such as radiation intensity, field strength, radiated power, etc., as a function of spherical coordinates which are specified by the elevation angle θ and the azimuth angle φ . More specifically, it is a plot of the power radiated from an antenna per unit solid angle which is nothing but the radiation intensity of an antenna. The radiation properties are measured in the far field region. For an antenna with largest dimension D , the far field region is given by distance equal to or greater than $2D^2/\lambda$, where λ is wavelength. Radiation patterns are generally described in terms of E and H plane pattern.

The E -plane (or H -plane) is defined as the plane containing the electric (or magnetic) field vector and the direction of propagation. The normalized far-field radiation patterns of all differently shaped FRA are shown in Figs. 8(a)–(f), respectively. The radiation characteristics show that the radiation is in broadside direction. Beam width is more in E -plane for cylindrical and cuboid compared to H -plane. However, H -plane beam width is more in triangular FRA. Further it can be observed that the maximum radiation is in the direction 324° and 326° respectively for cylindrical and cuboid FRA in E -plane and 351° in H -plane of triangular FRA. This deviation in the direction of maximum radiation from 0 (360°) to $324^\circ/326^\circ/351^\circ$ is due to the relative permeability (μ_r), which is greater than unity.

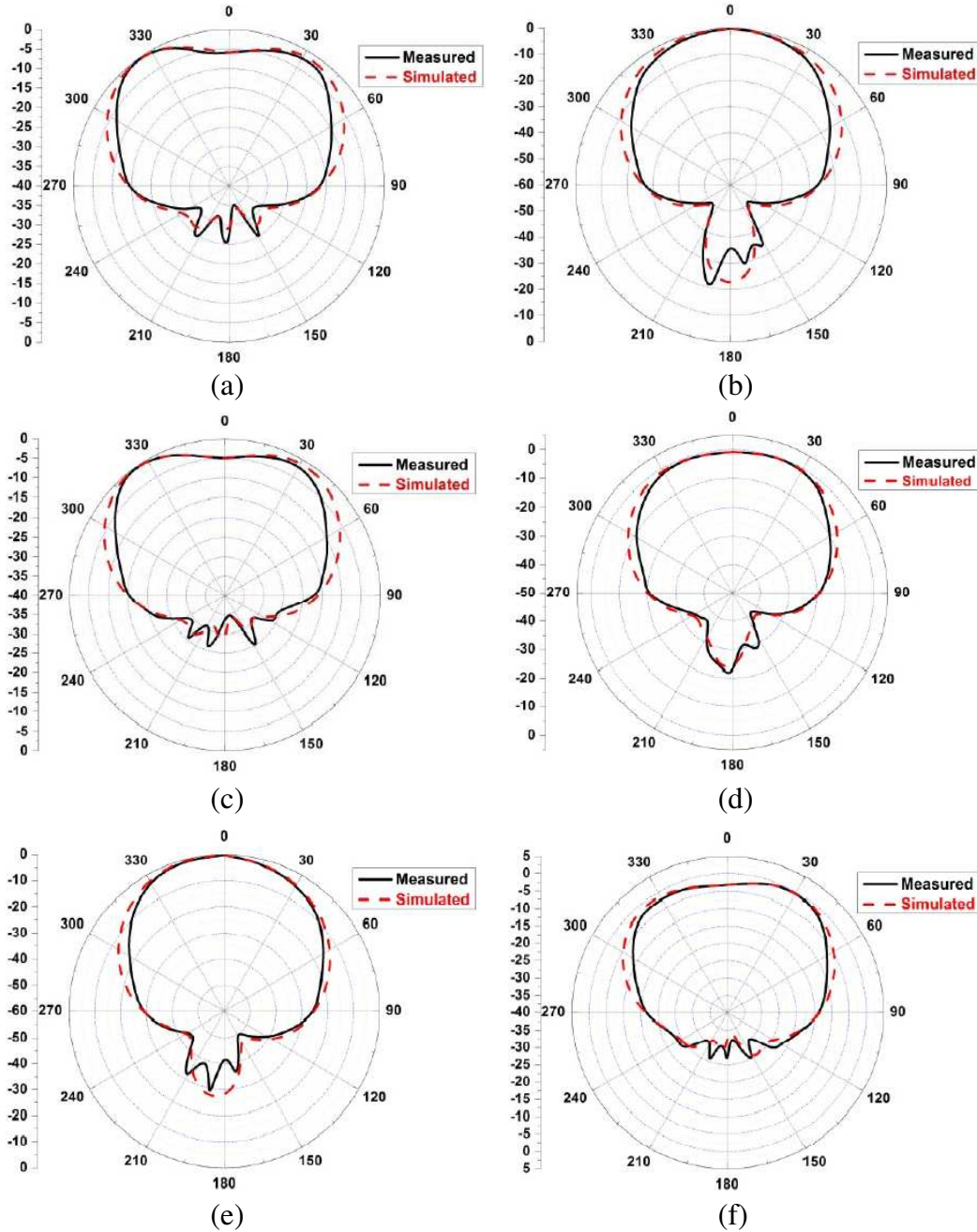


Figure 8. Far field radiation pattern of cylindrical FRA: (a) $\varphi = 0^\circ$, (b) $\varphi = 90^\circ$, cuboid FRA: (c) $\varphi = 0^\circ$, (d) $\varphi = 90^\circ$ and triangular FRA: (e) $\varphi = 0^\circ$, (f) $\varphi = 90^\circ$.

The most important parameter that describes the performance of an antenna is gain. This parameter is closely related to the directivity of the antenna. We know that the directivity is how much an antenna concentrates energy in one direction in preference to radiation in other directions, the gain is the amount of power that can be achieved in one direction at the expense of the power lost in the others. There are various techniques to measure the gain. The method used is two-antenna method, which utilizes two identical antennas for transmitting and receiving [95]. The gain can be calculated as

$$(G_{or})_{dB} = (G_{ot})_{dB} = \frac{1}{2} \left[20 \log_{10} \left(\frac{4\pi R}{\lambda} \right) + 10 \log_{10} \left(\frac{P_r}{P_t} \right) \right] \quad (31)$$

where,

$$G_{or} = \text{gain of receiving antenna (dB)},$$

G_{ot} = gain of transmitting antenna (dB),

R = antenna separation (m),

λ = operating wave length (m),

P_r = received power (W),

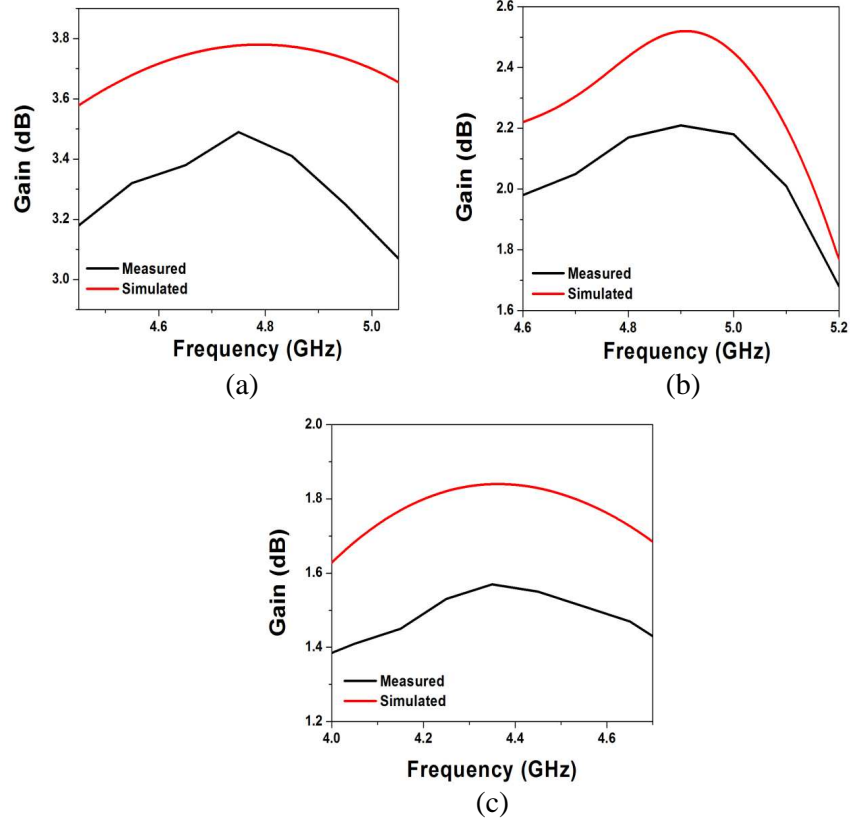


Figure 9. Variation of gain w.r.t frequency. (a) Cylindrical FRA, (b) cuboid FRA and (c) triangular FRA.

Table 3. Simulated and measured antenna characteristics of different shaped FRA.

	Cylindrical Shaped		Cuboid Shaped		Triangular Shaped	
	Simulated	Measured	Simulated	Measured	Simulated	Measured
Resonant frequency (GHz)	4.79	4.74	4.91	4.89	4.36	4.32
Reflection loss (S_{11}) dip (dB)	-33	-31	-42	-35	-14.5	-15
Bandwidth (GHz)	4.61 – 5	4.56 – 4.94	4.69 – 5.2	4.64 – 5.09	4.24 – 4.5	4.21 – 4.47
Return loss bandwidth	8.14%	8.02%	10.39%	9.2%	5.96 %	6.01%
VSWR	1.09	1.21	1.02	1.16	1.56	1.79
Gain (dB)	3.78 at 324°	3.49 at 324°	2.52 at 326°	2.21 at 326°	1.84 at 351°	1.57 at 351°
Antenna Efficiency	68.14%	65.29%	71.42%	66.83%	52.68%	49.37%
3-dB Beam-width (HPBW)						
<i>E</i> -plane	105°	80°	105°	76°	56°	46°
<i>H</i> -plane	68°	51°	91°	76°	104°	91°

P_t = transmitted power (W).

The Variation of gain w.r.t frequency of all differently shaped FRA is shown in Figs. 9(a)–(c), respectively.

Some of the antenna parameters are tabulated in the Table 3 for different shaped FRA. It can be seen that there is a good agreement in the measured and simulated result.

4. CONCLUSION

It can be concluded that single phase $\text{Ni}_{0.2}\text{Cu}_x\text{Zn}_{0.8-x}\text{Fe}_2\text{O}_4$ (where $x = 0, 0.2, 0.4, 0.6$ and 0.8), nanoparticles have been successfully synthesized by using auto-combustion sol-gel method with an average particle size 8–20 μm . SEM study revealed the formation of dense ceramics with different dimension grain also is homogeneously distributed. It has been found that the sintering temperature of ceramics was reduced from 1200°C to 1000°C by substitution of Cu in $\text{Ni}_{0.2}\text{Zn}_{0.8}\text{Fe}_2\text{O}_4$. The grain size of ceramics found to be increasing with increase in Cu-content. Raman spectroscopy showed the presence of symmetric and asymmetric stretching as well as symmetric bending in the materials. FTIR spectroscopy showed intrinsic vibrations of both tetrahedral and octahedral groups in the structure. The microwave dielectric constant and quality factor were measured by the method as proposed by Hakki-Coleman. The microwave dielectric constant varied from 7.474 to 8.132 and the value of τ_f changed from $-75.85 \text{ ppm}/^\circ\text{C}$ to $-32.12 \text{ ppm}/^\circ\text{C}$ with increase in Cu-content. This type of variation was attributed to change in ionic polarizability as well as cell volume. The variation in $Q \times f$ values was attributed to the inhomogeneous grain growth in the sample. The calculated permeability increases with increase in Cu-content within the range 2.1085 to 2.7138. Using this sample, three shapes (cylindrical, cuboid and triangular) of microwave DRAs with co-axial probe feeding mechanisms have been designed; their antenna behaviors have been studied experimentally as well as through simulations. Good agreement is achieved between the measured and simulated results. Maximum bandwidth 450 MHz and gain 3.49 dB was found with cuboid and cylindrical structure respectively.

REFERENCES

1. Reaney, I. M. and D. Iddles, "Microwave dielectric ceramics for resonators and filters in mobile phone networks," *J. Am. Ceram. Soc.*, Vol. 89, 2063–2072, 2006.
2. Cava, R. J., "Dielectric materials for applications in microwave communications," *J. Mater. Chem.*, Vol. 11, 54–62, 2001.
3. Rajput, S. S., S. Keshri, V. R. Gupta, N. Gupta, V. Bovtun, and J. Petzelt, "Design of microwave dielectric resonator antenna using MZTO-CSTO composite," *Ceramics International*, Vol. 38, No. 3, 2355–2362, 2012.
4. Hunter, C., L. Billonet, B. Jarry, and P. Gullion, "Microwave filters-applications and technology," *IEEE Trans. on Microw. Theory and Tech.*, Vol. 50, No. 3, 794–805, 2002.
5. Rajput, S. S. and S. Keshri, "Structural, vibrational and microwave dielectric properties of $(1-x)\text{Mg}_{0.95}\text{Co}_{0.05}\text{TiO}_3 - (x)\text{Ca}_{0.8}\text{Sr}_{0.2}\text{TiO}_3$ ceramic composites," *J. Alloys Compd.*, Vol. 581, 223–229, 2013.
6. Luk, K. M. and K. W. Leung, *Dielectric Resonator Antennas*, Research Studies Press Ltd., Baldock, England, 2002.
7. Fehine, P. B. A., R. S. T. Moretzsohn, R. C. S. Costa, J. Derov, J. W. Stewart, A. J. Drehman, C. Junqueira, and A. S. B. Sombra, "Magneto-dielectric properties of the $\text{Y}_3\text{Fe}_5\text{O}_{12}$ and $\text{Gd}_3\text{Fe}_5\text{O}_{12}$ dielectric ferrite resonator antennas," *Microwave Opt. Technol. Lett.*, Vol. 50, No. 11, 2852–2857, 2008.
8. Parida, S., S. K. Rout, N. Gupta, and V. R. Gupta, "Solubility limits and microwave dielectric properties of $\text{Ca}(\text{Zr}_x\text{Ti}_{1-x})\text{O}_3$ solid solution," *J. Alloys Compd.*, Vol. 546, 216–223, 2013.
9. Parida, S., S. K. Rout, V. Subramanian, P. K. Barhai, N. Gupta, and V. R. Gupta, "Structural, microwave dielectric properties and dielectric resonator antenna studies of $\text{Sr}(\text{Zr}_x\text{Ti}_{1-x})\text{O}_3$ ceramics," *J. Alloys Compd.*, Vol. 528, 126–134, 2012.

10. Louzir, A., P. Minard, and J. F. Pintos, "Parametric study on the use of magneto-dielectric materials for antenna miniaturization," *IEEE Antennas and Propagation Society International Symposium (APSURSI)*, Vol. 978, No. 1, 1–4, 2010.
11. Hansen, R. C. and M. Burke, "Antennas with magneto-dielectrics," *Microwave Opt. Technol. Lett.*, Vol. 26, No. 2, 75–78, 2000.
12. Albuquerque, A. S., J. D. Ardisson, W. A. A. Macedo, and M. C. M. Alves, "Nanosized powders of NiZn ferrite: Synthesis, structure, and magnetism," *J. Appl. Phys.*, Vol. 87, 4352–4357, 2000.
13. Goldman, A., "Magnetic ceramics (ferrites). In: Engineered materials handbook — 'Ceramics and glasses'," *ASM International, The Materials Information Society*, Vol. 4, 1161, 1991.
14. Ebnabbasi, K., M. Mohebbi, and C. Vittoria, "Coaxial line technique to measure constitutive parameters in magnetolectric ferrite materials," *IEEE Micro. Wireless Comp. Letters*, Vol. 23, No. 9, 504–506, 2013.
15. Ebnabbasi, K., M. Mohebbi, and C. Vittoria, "Strong magnetolectric coupling in hexaferrites at room temperature," *J. Appl. Phys.*, Vol. 113, 17C707-1–17C707-3, 2013.
16. Souriou, D., J. L. Mattei, A. Chevalier, and P. Queffelec, "Influential parameters on electromagnetic properties of nickel-zinc ferrites for antenna miniaturization," *J. Appl. Phys.*, Vol. 107, 09A518, 2010.
17. Ebnabbasi, K., M. Mohebbi, and C. Vittoria, "Magnetolectric effects at microwave frequencies on Z-type hexaferrite," *App. Phy. Letters*, Vol. 101, 062406-1–062406-3, 2012.
18. Ebnabbasi, K., Y. Chen, A. Geiler, V. Harris, and C. Vittoria, "Magneto-electric effects on Sr Z-type hexaferrite at room temperature," *J. Appl. Phys.*, Vol. 111, 07C719-1–07C719-3, 2012.
19. Mohebbi, M., K. Ebnabbasi, and C. Vittoria, "In-situ deposition of C-axis oriented barium ferrite films for microwave applications," *IEEE Trans. on Magn.*, Vol. 49, No. 7, 4207–4209, 2013.
20. Adam, J. D., S. V. Krishnaswamy, S. H. Talisa, and K. C. Yoo, "Thin-film ferrites for microwave and millimeter-wave applications," *J. Magn. Magn. Mater.*, Vol. 83, No. 1–3, 419–424, 1990.
21. Yang, G.-M., J. Lou, O. Obi, and N. X. Sun, "Novel compact and low-loss phase shifters with magnetodielectric disturber," *IEEE Micro. Wireless Comp. Letters*, Vol. 21, No. 5, 240–242, 2011.
22. Kong, L. B., Z. W. Li, G. Q. Lin, and Y. B. Gan, "Ni-Zn ferrites composites with almost equal values of permeability and permittivity for low-frequency antenna design," *IEEE Trans. on Magn.*, Vol. 43, No. 1, 6–10, 2007.
23. Yang, G. M., "Tunable miniaturized RF devices on magneto-dielectric substrates with enhanced performance," Northeastern University, Boston, Massachusetts, Apr. 2010.
24. Mohit, K., V. R. Gupta, N. Gupta, and S. K. Rout, "Structural and microwave characterization of $\text{Ni}_{0.2}\text{Co}_x\text{Zn}_{0.8-x}\text{Fe}_2\text{O}_4$ for antenna applications," *Ceramics International*, Vol. 40, 1575–1586, 2014.
25. Teo, M. L. S., L. B. Kong, Z. W. Li, G. Q. Lin, and Y. B. Gan, "Development of magneto-dielectric materials based on Li-ferrite ceramics: II. DC resistivity and complex relative permittivity," *J. Alloy Compd.*, Vol. 459, 567–575, 2008.
26. Slick, P. I., *Ferromagnetic Materials*, E. P. Wohlfarth, Ed., Vol. 2, 196, North-Holland, Amsterdam, 1980.
27. Albuquerque, A. S., J. D. Ardisson, W. A. A. Macedo, and M. C. M. Alves, "Nanosized powders of NiZn ferrite: Synthesis, structure, and magnetism," *J. Appl. Phys.*, Vol. 87, 4352–4357, 2000.
28. Pathan, A. N., K. Sangshetti, and A. A. G. Pangal, "Synthesis, characterisation and magnetic studies of $\text{Co}_{0.4}\text{Zn}_{0.4-x}\text{Cu}_x\text{Fe}_2\text{O}_4$ nanoparticles," *Nanotechnology and Nanoscience*, Vol. 1, No. 1, 8–12, 2010.
29. Su, H., X. Tang, H. Zhang, Z. Zhong, and J. Shen, "Sintering dense NiZn ferrite by two-step sintering process," *J. Appl. Phys.*, Vol. 109, 07A501, 2011.
30. Su, H., X. Tang, H. Zhang, Y. Jing, F. Bai, and Z. Zhong, "Low-loss NiCuZn ferrite with matching permeability and permittivity by two-step sintering process," *J. Appl. Phys.*, Vol. 113, 17B301, 2013.

31. Naser, M. G., E. B. Saion, M. Hashim, A. H. Shaari, and H. A. Ahangar, "Synthesis and characterization of zinc ferrite nanoparticles by a thermal treatment method," *Solid State Communications*, Vol. 151, 1031–1035, 2011.
32. Joseyphus, R. J., C. N. Chinnasamy, B. Jeyadevan, A. Kasuya, K. Shinoda, A. Narayanasamy, and K. Tohji, "Synthesis of ferrite nanoparticles through aqueous process for biomedical applications," *Proceedings, 1st International Workshop on Water Dynamics Tohoku University*, 51–53, Sendai, Japan, Mar. 17–19, 2004.
33. Todaka, Y., M. Nakamura, S. Hattori, K. Tsuchiya, and M. Umemoto, "Synthesis of ferrite nanoparticles by mechanochemical processing using a ball mill," *Materials Transactions*, Vol. 44, 277–284, 2003.
34. Li, S., L. Liu, V. T. John, C. J. O'Connor, and V. G. Harris, "Cobalt-ferrite nanoparticles: Correlations between synthesis procedures, structural characteristics and magnetic properties," *IEEE Trans. on Magn.*, Vol. 37, 2350–2352, 2001.
35. Raval, A. M., N. R. Panchal, and R. B. Jotania, "Structural studies of co-spinel ferrite synthesized by an auto combustion method," *Journal of Analytical Techniques*, Vol. 1, 01–02, 2010.
36. Christou, A. and J. F. Crider, "The strengthening of Ti-55 at. % Ni by formation of a Ti_2Ni_3 intermetallic phase," *Journal of materials science*, *J. Material Sc.*, Vol. 7, No. 4, 479–480, 1972.
37. Munir, Z. A., "Synthesis of high temperature materials by self-propagating combustion methods," *Fenmo Yejin Jishu/Powder Metallurgy Technology*, Vol. 6, No. 1, 1–24, 1988.
38. Sutka, A. and G. Mezinskas, "Sol-gel auto-combustion synthesis of spinel-type ferrite nanomaterials," *Front. Mater. Sci.*, Vol. 6, 128–141, 2012.
39. Thant, A. A., S. Srimala, P. Kaung, M. Itoh, O. Radzali, and M. N. Ahmad Fauzi, "Low temperature synthesis of $MgFe_2O_4$ soft ferrite nanocrystallites," *J. Australian Ceram. Soc.*, Vol. 46, 11–14, 2010.
40. Huang, C.-L., J.-J. Wang, and C.-Y. Huang, "Sintering behavior and microwave dielectric properties of nano alpha-alumina," *Materials Letters*, Vol. 59, 3746–3749, 2005.
41. Huang, C.-L., J.-J. Wang, and C.-Y. Huang, "Microwave dielectric properties of sintered alumina using nano-scaled powders of a Alumina and TiO_2 ," *J. Am. Ceram. Soc.*, Vol. 90, 1487–1493, 2007.
42. Zahi, S., "Synthesis, permeability and microstructure of the optimal nickel-zinc ferrites by sol-gel route," *J. Electromagnetic Analysis & Applications*, Vol. 2, 56–62, 2010.
43. Goldman, A., *Modern Ferrite Technology*, Van Nostrand Reinhold, New York, 1990.
44. Slemon, G. R., *Magnetolectric Devices*, Wiley, New York, 1966.
45. Bae, S. Y., H. J. Jung, C. S. Kim, and Y. J. Oh, "Magnetic properties of sol-gel derived Ni-Zn ferrite thin films," *J. de Phys. IV JP*, Vol. 8, No. 2, 261–264, 1998.
46. Lee, J. S., B. I. Lee, and S. K. Joo, "Effects of process parameters on structure and magnetic properties of sputtered Ni-Zn ferrite thin films," *IEEE Trans. on Magn.*, Vol. 35, 3415–3417, 1999.
47. Qian, Z., G. Wang, J. M. Sivertsen, and J. H. Judy, "Ni-Zn ferrite thin films prepared by facing target sputtering," *IEEE Trans. on Magn.*, Vol. 33, 3748–3750, 1997.
48. Kiyomura, T. and M. Gomi, "Room-temperature epitaxial growth of Ni-Zn ferrite thin films by pulsed laser deposition in high vacuum," *Jpn. J. Appl. Phys. Part 2: Lett.*, Vol. 36, L1000–L1002, 1997.
49. Verma, A. and D. C. Dube, "Processing of nickel-zinc ferrites via the citrate precursor route for high-frequency applications," *J. Am. Ceram. Soc.*, Vol. 88, 519–523, 2005.
50. Nakamura, T., "Low-temperature sintering of Ni-Zn-Cu ferrite and its permeability spectra," *J. Magn. Magn. Mater.*, Vol. 168, 285–291, 1997.
51. Rahman, I. Z. and T. T. Ahmed, "A study on Cu substituted chemically processed Ni-Zn-Cu ferrites," *J Magn Magn Mater.*, Vol. 290–291, 1576–1579, 2005.
52. Apesteguy, J. C., A. Damiani, D. D. Giovanni, and S. E. Jacobo, "Microwave-absorbing characteristics of epoxy resin composites containing nanoparticles of NiZn- and NiCuZn-ferrites," *Physica B*, Vol. 404, No. 18, 2713–2716, 2009.

53. Mohit, K., S. K. Rout, S. Parida, G. P. Singh, S. K. Sharma, S. K. Pradhan, and I. W. Kim, "Structural, optical and dielectric studies of $\text{Ni}_x\text{Zn}_{1-x}\text{Fe}_2\text{O}_4$ prepared by autocombustion route," *Physica B*, Vol. 407, 935–942, 2012.
54. Cullity, B. D., *Element of X-ray Diffraction*, 2nd Edition, Wesley Publication Company Inc., 1978.
55. Smit, J. and H. P. J. Wijn, *Ferrites*, John Wiley, New York, 1959.
56. Hakki, B. W. and P. D. Coleman, "A dielectric resonator method of measuring inductive capacities in the millimeter range," *IRE Trans. on Microw. Theory Tech.*, Vol. 8, No. 4, 402–410, 1960.
57. Courtney, W. E., "Analysis and evaluation of a method of measuring the complex permittivity and permeability microwave insulators," *IEEE Trans. on Microw. Theory and Tech.*, Vol. 18, No. 8, 476–485, 1970.
58. Sebastian, M. T., *Dielectric Materials for Wireless Communication*, Elsevier Publication, 2008.
59. Krupka, J., "Frequency domain complex permittivity measurements at microwave frequencies," *Meas. Sci. Technol.*, Vol. 16, R1–R16, 2005.
60. Krupka, J., K. Derzakowski, B. Riddle, and J. B. Jarvis, "A dielectric resonator for measurements of complex permittivity of low loss materials as a function of temperature," *Meas. Sci. Technol.*, Vol. 9, 1751–1756, 1998.
61. Chen, L. F., C. K. Ong, C. P. Neo, V. V. Varadan, and V. K. Varadan, *Microwave Electronics: Measurement and Materials Characterization*, 209, John Wiley & Sons Ltd., The Atrium, Southern Gate, Chichester, West Sussex PO19 8SQ, England, 2004.
62. Kobayashi, Y. and S. Tanaka, "Resonant modes of a dielectric rod resonator short-circuited at both ends by parallel conducting plates," *IEEE Trans. on Microw. Theory and Tech.*, Vol. 28, No. 10, 1077–1085, 1980.
63. Parida, S., S. K. Rout, L. S. Cavalcante, E. Sinha, M. S. Li, V. Subramanian, N. Gupta, V. R. Gupta, J. A. Varela, and E. Longo, "Structural refinement, optical and microwave dielectric properties of BaZrO_3 ," *Ceramics International*, Vol. 38, No. 3, 2129–2138, 2012.
64. Moreira, M. L., P. G. C. Buzolin, V. M. Longo, N. H. Nicoletti, J. R. Sambrano, M. S. Li, J. A. Varela, and E. Longo, "Joint experimental and theoretical analysis of order-disorder effects in cubic BaZrO_3 assembled nanoparticles under decaoctahedral shape," *J. Phys. Chem. A.*, Vol. 115, 4482–4490, 2011.
65. Kobayashi, Y. and M. Katoh, "Microwave measurement of dielectric properties of low-loss materials by the dielectric rod resonator method," *IEEE Trans. on Microw. Theory and Tech.*, Vol. 33, No. 7, 586–592, 1985.
66. Afsar, M. N., J. R. Birch, and R. N. Clarke, "The measurement of the properties of materials," *IEEE Trans. on Microw. Theory and Tech.*, Vol. 25, No. 1, 183–199, 1977.
67. De Paula, A. L., M. C. Rezende, and J. J. Barroso, "Experimental measurements and numerical simulation of permittivity and permeability of teflon in X band," *J. Aerosp. Technol. Manag. São José dos Campos.*, Vol. 3, No. 1, 59–64, 2011.
68. Kajfez, D. and P. Guillon, *Dielectric Resonators*, The Artech House Microwave Library, Norwood, MA, 1986.
69. Petosa, A., A. Ittipiboon, Y. M. M. Antar, and D. Roscoe, "Recent advances in dielectric-resonator antenna technology," *IEEE Antennas Propag. Mag.*, Vol. 40, 35–48, 1998.
70. Junker, G. P., A. W. Glisson, and A. A. Kishk, "Input impedance of dielectric resonator antennas top loaded with high permittivity and conducting disks," *Microw. Opt. Technol. Lett.*, Vol. 9, 204–207, 1995.
71. Junker, G. P., A. A. Kishk, A. W. Glisson, and D. Kajfez, "Effect of an air gap around the coaxial probe exciting a cylindrical dielectric resonator antenna," *Electron. Lett.*, Vol. 30, 177–178, 1994.
72. Mongia, R. K. and A. Ittipiboon, "Theoretical and experimental investigations on rectangular dielectric resonator antennas," *IEEE Trans. on Antenna and Propag.*, Vol. 45, No. 9, 1348–1356, 1997.
73. Peng, Z., H. Wang, and X. Yao, "Dielectric resonator antennas using high permittivity ceramics," *Ceramics International*, Vol. 30, 1211–1214, 2004.

74. Luk, K. M. and K. W. Leung, *Dielectric Resonator Antennas*, Research Studies Press Ltd., Hertfordshire, UK, 2002.
75. Kumari, R., K. Parmar, and S. K. Behera, "Conformal patch fed stacked triangular dielectric resonator antenna for wlan applications," *IEEE Int. Conf. Emerging Trends in Robotics and Comm. Tech.*, 104–107, Sathyabama University, Chennai, Dec. 3–5, 2010.
76. Grabovickic, R., "Accurate calculations of geometrical factors of Hakki-Coleman shielded dielectric resonators," *IEEE Trans. on Appl. Supercond*, Vol. 9, 4607–4612, 1999.
77. Hwang, C. C., J. S. Tsai, and T. H. Huang, "Combustion synthesis of Ni-Zn ferrite by using glycine and metal nitrates — Investigations of precursor homogeneity, product reproducibility, and reaction mechanism," *Mater. Chem. Phys.*, Vol. 93, 330–336, 2005.
78. Kugimiya, K. and H. Steinfink, "Influence of crystal radii and electronegativities on the crystallization of AB_2X_4 stoichiometries," *J. Inorganic Chem.*, Vol. 7, 1762–1770, 1968.
79. Modi, K. B., P. V. Tanna, S. S. Laghate, and H. H. Joshi, "The effect of Zn^{+2} substitution on some structural properties of $CuFeCrO_4$ system," *J. Mater. Sci. Lett.*, Vol. 19, 1111–1113, 2000.
80. Sathishkumar, G., C. Venkataraju, and K. Sivakumar, "Structural and dielectric studies of nickel substituted cobalt-zinc ferrite," *Mat. Sci. App.*, Vol. 1, 19–24, 2010.
81. Scherrer, P. and G. Nachricht, "Bestimmung der grösse und der innerenstruktur von kolloidteilchen mittels röntgenstrahlen, nachrichten von der gesellschaft der wissenschaften, göttingen," *Mathematisch-Physikalische Klasse*, Vol. 2, 98–100, 1918.
82. Shebanova, O. N. and P. Lazer, "Raman spectroscopic study of magnetite ($FeFe_2O_4$): A new assignment for the vibrational spectrum," *J. State Chem.*, Vol. 174, 424–430, 2003.
83. Prince, E., *Mathematical Technique in Crystallography and Material Science*, Springer Verlag, New York, Heidelberg, Berlin, 1982.
84. Wang, Z., D. Schiferl, Y. Zhao, and H. S. C. O'Neill, "High pressure Raman spectroscopy of spinel-type ferrite $ZnFe_2O_4$," *J. Phys. Chem. Solids*, Vol. 64, 2517–2523, 2003.
85. Waldron, R. D., "Infrared spectra of ferrites," *Phys. Rev.*, Vol. 99, 1727–1735, 1955.
86. Hafner, S., "Ordnung/unordnung und ultrarotabsorption IV. Die absorption einiger metalloxyde mit spinellstruktur," *Z. Krist.*, Vol. 115, 331–358, 1961.
87. Ostos, C., L. Mestres, M. L. Martínez-Sarrión, J. E. García, A. Albareda, and R. Perez, "Synthesis and characterization of A-site deficient rare-earth doped $BaZr_xTi_{1-x}O_3$ perovskite-type compounds," *Solid State Sci.*, Vol. 11, 1016–1022, 2009.
88. Tsurumi, T., T. Teranishi, S. Wada, H. Kakemoto, M. Nakada, and J. Akedo, "Wide range dielectric spectroscopy of $SrTiO_3$ - $SrZrO_3$ solid solution," *15th IEEE International Symposium on the Applications of Ferroelectrics, isaf'06*, 1–8, USA, 2006.
89. Lee, C. T., C. T. Chen, C. Y. Huang, and C. J. Wang, "Microwave dielectric properties of $(Ba_{1-x}Mg_x)_5Nb_4O_{15}$ ceramics," *Jap. J. Appl. Phys.*, Vol. 47, No. 6, 4634–4637, 2008.
90. Shannon, R. D., "Dielectric polarizabilities of ions in oxides and fluorides," *J. Appl. Phys.*, Vol. 73, 348–366, 1993.
91. Grimes, N. W. and R. W. Grimes, "Dielectric polarizability of ions and the corresponding effective number of electrons," *J. Phys.: Condens. Matter*, Vol. 10, 3029–3034, 1998.
92. Yoon, S. H., D. W. Kim, S. Y. Cho, and K. S. Hong, "Investigation of the relations between structure and microwave dielectric properties of divalent metal tungstate compounds," *J. European Ceramic Society*, Vol. 26, 2051–2054, 2006.
93. Schenck, J. F., *General Electric Corporate Research and Development Center*, 12309, Schenectady, New York, 1996.
94. Rajput, S. S., S. Keshri, and V. R. Gupta, "Microwave dielectric properties of $(1-x)Mg_{0.95}Zn_{0.05}TiO_3-(x)Ca_{0.6}La_{0.8/3}TiO_3$ ceramic composites," *J. Alloys Compd.*, Vol. 552, 219–226, 2013.
95. Balanis, C. A., *Antenna Theory Analysis and Design*, John Wiley & Sons, Inc., 2005.